February 2005 • NREL/SR-520-37578

Subcontractor Report

Efficiency Improvement of Crystalline Solar Cells

Final Subcontract Report
October 2001–December 2004

E.R. Weber
University of California, Berkeley
Berkeley, California

National Renewable Energy Laboratory
1617 Cole Boulevard, Golden, Colorado 80401-3393
303-275-3000 • www.nrel.gov

Operated for the U.S. Department of Energy
Office of Energy Efficiency and Renewable Energy
by Midwest Research Institute • Battelle

Contract No. DE-AC36-99-GO10337

February 2005 • NREL/SR-520-37578

Efficiency Improvement of Crystalline Solar Cells

Final Subcontract Report
October 2001–December 2004

E.R. Weber
University of California, Berkeley
Berkeley, California

NREL Technical Monitor: R. Matson

Prepared under Subcontract No. AAT-2-31605-03

National Renewable Energy Laboratory
1617 Cole Boulevard, Golden, Colorado 80401-3393
303-275-3000 • www.nrel.gov

Operated for the U.S. Department of Energy
Office of Energy Efficiency and Renewable Energy
by Midwest Research Institute • Battelle

Contract No. DE-AC36-99-GO10337

Table of Contents

List of Figures

A. Motivation and objectives of research

Crystalline silicon (c-Si) accounts for over 90% of the total photovoltaic (PV) production worldwide and fuels the average 30% industry-wide growth rate. Solar cells produced from high-purity single-crystalline silicon have achieved nearly 25% laboratory efficiencies; high-purity multicrystalline silicon (mc-Si) material has achieved about 20%, whereas mc-Si produced from lower-quality feedstock, although much cheaper, typically results in solar cells with efficiencies between 12-15%. To be competitive on the energy market dominated by hydroelectric, nuclear, and fossil fuel power plants, the price per kWh of the installed PV modules should continue decreasing. To achieve the lowest possible production cost combined with acceptable efficiency, many PV companies prefer to work with the low-cost mc-Si, cognizant that the loss of efficiency relative to single-crystalline silicon is offset by the lower production cost of solar cells.

The lower efficiency of mc-Si solar cells is caused by the presence of impurities and structural defects, which severely degrade the electrical properties of the material. If control over efficiency-limiting defects in mc-Si were to be achieved without substantially raising the production costs, then a significant reduction of cost per kWh could be realized. Such an improvement would further increase the competitive advantage of mc-Si, hastening the introduction of PV into the mainstream energy market. A formidable challenge to removing or passivating efficiency-limiting defects, especially metal-related ones, lies in the fact that until very recently, a comprehensive understanding of their chemical state, distribution, and impact on cell efficiency was lacking. This was mainly because these defects can be very small (often tens or hundreds of nanometers in size) and separated by comparatively large distances (often several microns), making their study very challenging for conventional analytical techniques.

The objective of this subcontract was to gain fundamental physical understanding of the transition metal related defects in PV-grade multicrystalline silicon through elucidating the pathways of their introduction into solar cells, their chemical state and distribution within mc-Si, and their interaction with structural defects. The further objective was to assess the possibilities of reduction of detrimental impact of these defect clusters on the cell performance via defect engineering.

B. Approach

The approach used in this subcontract was to use unique analytical tools available at Berkeley to perform systematic fundamental physical studies of distribution and chemical state of metal clusters in a variety of multicrystalline silicon materials.

Two analytical techniques were essential for the success of this project. The total metal concentration in the areas of multicrystalline silicon with high and low lifetime was determined by neutron activation analysis, the technique which involves irradiation of the samples with neutrons in a nuclear reactor and analysis of its residual radioactivity. The distribution and chemical state of metal clusters was characterized by synchrotron radiation based x-ray microscopes available at the Advanced Light Source (Beamlines 10.3.1 and 10.3.2) at Lawrence Berkeley National Laboratory and Advanced Photon Source (Beamlines 2-ID-D and 20-ID-B) at Argonne National Laboratory. At these beamlines, x-rays can be focused into spot sizes of 200 nm to 5 μm in diameter. A small beam size, high flux, and ultra-low Bremsstrahlung background allow one to achieve the high sensitivity necessary to detect very small metal clusters. For typical experimen-

tal conditions with a 200 nm diameter beam and an accumulation time of 1 second, we have detected iron silicide clusters of radius 23±5 nm, while the noise-limited detection limit for the same conditions was estimated to be 16±3 nm. After metal-rich clusters of interest were located via microprobe x-ray fluorescence (μ-XRF), their chemical state (e.g., oxide vs silicide) was assessed via X-ray absorption microspectroscopy (μ-XAS). By using a monochromator to vary the energy of the X-ray beam with an energy resolution of 1 eV or better, the X-ray absorption spectrum of the metal particle was compared against the absorption spectra of commercially available standard materials such as metal-oxides or metal-silicides. Recombination activity of metal clusters could be assessed by in-situ x-ray beam induced current measurements (XBIC).

We analyzed and compared mc-Si materials grown using different technologies, including samples of sheet, cast, and ribbon-grown mc-Si, as well as multicrystalline silicon grown by the float zone technique at NREL. From these data, we were able to identify statistically meaningful trends, those material-specific as well as those generic to all mc-Si materials, in the distribution and properties of metal clusters, and their response to heat treatments and gettering.

C. Summary of major accomplishments

C.1. Identification of the dominant metal impurities in bad regions; Comparison of different growth techniques on terms of metal contamination *(tasks 1 and 3 of the phase 1 of the project)*.

Neutron activation analysis (NAA) was used to determine the total metal content in three types of commercially available multicrystalline silicon – Astropower sheet material, Baysix cast material, and EFG ribbon. Besides determination of the average metal concentration in each of these three types of material, we compared the metal contents of samples cleaved from the areas with relatively high ("good regions") and relatively low ("bad regions") minority carrier diffusion length for each of the three materials.

The NAA results are presented in the Tables I-IV below. The dominant metal impurities were found to be Fe (6×10^{14} cm^{-3} to 1.5×10^{16} cm^{-3}, depending on the material), Ni (up to 1.8×10^{15} cm^{-3}), Co (1.7×10^{12} cm^{-3} to 9.7×10^{13} cm^{-3}), Mo (6.4×10^{12} cm^{-3} to 4.6×10^{13} cm^{-3}), and Cr (1.7×10^{12} cm^{-3} to 1.8×10^{15} cm^{-3}) (see Table I). The primary contaminants in all three materials were Fe, Ni, and Cr, which may be an indication of contamination with stainless steel. Copper was also detected (less than 2.4×10^{14} cm^{-3}), but its concentration could not be accurately determined because of a very short decay time of the corresponding radioactive isotope.

Remarkably, the total concentration of transition metals observed in all three mc-Si materials was much higher than necessary to explain the minority carrier lifetime degradation in these materials: the average concentration of iron alone was at least ten times higher than it would be sufficient, if all iron were in the interstitial state, to account for the carrier recombination responsible for the measured minority carrier diffusion length. Therefore, either transition metals are present in relatively recombination inactive chemical/structural state, or they are extremely inhomogeneously distributed in the wafer, or both.

Analysis of samples cleaved from the areas with high and low minority carrier diffusion length (Tables II-IV) revealed that the difference in metal concentration in "good" and "bad" areas is small. Only gold was consistently found in the "bad" areas in 1.5 to 5 times higher concentrations than in the "good" areas of all three materials. The rest of the metals detected by NAA showed either no trend at all, or, in some cases, metals were even found in slightly higher con-

centration in the "good" areas. Therefore, it is likely that it is not the total metal content but rather a variation in the spatial distribution and/or chemical/structural state of metals that leads to a change in their recombination properties.

Table I. Average metal concentration found by neutron activation analysis of three types of multicrystalline silicon material: Astropower (sheet technology), BaySix (cast), and EFG (ribbon growth). DL stands for "detection limit".

Element	ASTROPOWER (cm^{-3})	BaySix (cm^{-3})	EFG (cm^{-3})
Fe	1.50×10^{16}	4.00×10^{14}	6.00×10^{14}
Ni	1.80×10^{15}	*less than DL (3e14)*	*less than DL (1.1e14)*
Co	9.70×10^{13}	2.10×10^{13}	1.70×10^{12}
Cu	*less than DL (7.8×10^{12})*	*<2.4×10^{14}*	*<1.3×10^{14}*
Cr	1.80×10^{15}	1.00×10^{13}	1.70×10^{12}
Hf	*less than DL (1.8×10^{12})*	7.80×10^{12}	*less than DL (6.8×10^{11})*
Mo	4.60×10^{13}	1.50×10^{13}	6.40×10^{12}
W	2.00×10^{13}	*less than DL (2.2×10^{11})*	*less than DL (8×10^{10})*
Au	4.80×10^{11}	6.50×10^{10}	2.00×10^{10}
As	4.70×10^{13}	3.40×10^{12}	*less than DL (9.3×10^{10})*
Sb	2.40×10^{14}	1.70×10^{12}	1.20×10^{11}
Ga	2.50×10^{13}	*less than DL*	9.00×10^{12}

Table II. Metal concentration in the areas of EFG samples with higher than average ("good regions") and lower than average ("bad regions") minority carrier diffusion lengths. Due to different irradiation and counting conditions, the detection limits of this measurement run were lower than of the runs presented in Tables I, III, IV. Therefore, iron and some other metals were below the detection limits.

Element	"Good" areas (cm^{-3})	"Bad" areas (cm^{-3})
Cr	2.97×10^{12}	5.94×10^{11}
Mo	7.09×10^{13}	6.00×10^{13}
Sb	8.20×10^{10}	9.00×10^{10}
Au	5.00×10^{11}	3.00×10^{12}

Table III. Metal concentration in BaySix wafers with relatively high (middle of the ingot) and relatively low (bottom of the ingot) minority carrier diffusion length. DL stands for "detection limit".

Element	Sample A (middle of the ingot, better cell performance) (cm^{-3})	Sample B (bottom of the ingot, lower cell performance) (cm^{-3})
Ag	3×10^{12}	*less than DL (5×10^{11})*
Cr	1.9×10^{13}	*less than DL (3×10^{12})*
Fe	4.7×10^{14}	*less than DL (4.5×10^{14})*
Ni	*less than DL (3×10^{14})*	*less than DL (2.3×10^{14})*
Co	8×10^{12}	2.80×10^{13}
As	3.80×10^{12}	2.90×10^{12}
Sb	3.70×10^{11}	3.20×10^{12}
W	*less than DL (1×10^{11})*	*less than DL (3.6×10^{11})*
Au	1.50×10^{10}	1.20×10^{11}
Zr	3.3×10^{14}	3.5×10^{14}
Hf	1.40×10^{13}	*less than DL (1.1×10^{12})*
Cu	<1.6e14	<3.2×10^{14}
Se	2×10^{13}	4×10^{12}
Mo	1.50×10^{13}	*less than DL (5.4×10^{13})*

Table IV. Metal concentration in Astropower wafers with relatively high ("wafer A") and relatively low ("wafer B") minority carrier diffusion length areas.

Element	Wafer A (better cell performace) (cm^{-3})	Wafer B (lower cell performance) (cm^{-3})
Cr	3×10^{15}	5×10^{13}
Fe	1.6×10^{16}	8.7×10^{15}
Ni	2.8×10^{15}	*less than DL (5e15)*
Co	1.3×10^{14}	6.1×10^{13}
Cu	*less than DL (5e12)*	*less than DL (1e13)*
Ga	2×10^{12}	*less than DL(3e12)*
As	9×10^{13}	3.5×10^{12}
Zr	*less than DL (1.5×10^{15})*	*less than DL (4×10^{15})*
Hf	*less than DL (1.1×10^{12})*	*less than DL (3×10^{12})*
Mo	6×10^{13}	3×10^{13}
Sb	2×10^{13}	5×10^{14}
W	2×10^{13}	2×10^{13}
Au	3.5×10^{11}	4×10^{11}

C.2. Removal of metals from mc-Si by aluminum gettering; metals in bad regions which cannot be removed by aluminum gettering *(phase 1, task 2)*.

700 μm-thick CZ sample containing 10^6 cm^{-3} oxygen precipitates was intentionally contaminated with copper at 1200°C. A 5 μm aluminum layer was evaporated onto one surface of the sample through a wire mesh. Gettering anneal was performed at 800°C for 2 hours in forming gas ambient.

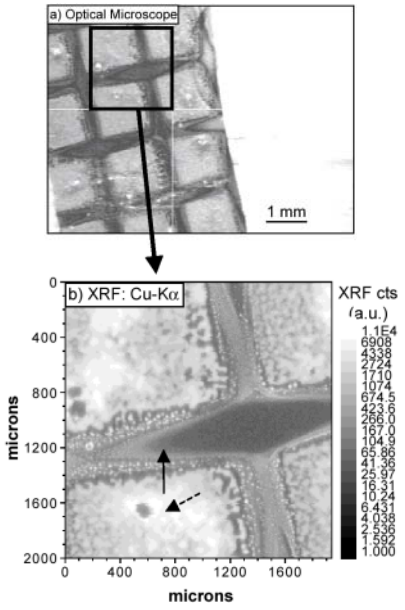

Fig. C.2.1. (a) Optical microscope image of the surface of a Cu-contaminated CZ-Si sample with 10^6 cm^{-3} oxygen precipitates. This sample was annealed at 800°C for 2 hours after squares of aluminum were evaporated onto the surface through a wire mesh. (b) Cu-Ka x-ray fluorescence microscopy image for the region highlighted in (a) shows the high concentration of Cu gettered to the thick Al squares (note log XRF scale), and the fine dusting of Cu in tiny Al particles between the squares, indicative that even a tiny bit of Al is a very effective getter of Cu. The dashed arrow denotes location of μ-EXAFS scans in Figure C.2.2

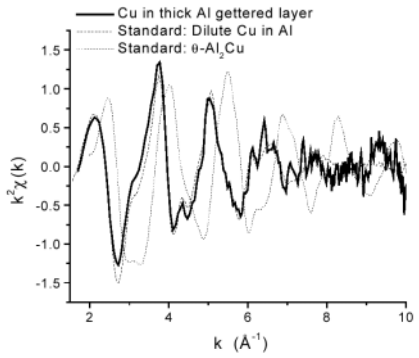

Fig. C.2.2. EXAFS of Cu gettered to thick regions of Al (dashed arrow in Fig. C.2.1b). Notice the good agreement with the standard material of dilute Cu dissolved in Al

μ-XRF mapping of the aluminum layer (Fig. C.2.1) revealed that copper was present only where aluminum was deposited through the wire mesh. Chemical identification performed by μ-XAS revealed that copper gettered to the thicker regions of Al (indicated by a dashed arrow in Fig. C.2.1b) had formed a dilute Cu solution in Al (Fig. C.2.2) identified in [M.A.Marcus and J.E.Bower, J.Appl.Phys. **82**, 3821 (1997)]. This confirms that the mechanism of segregation in aluminum is a higher metal solubility in the liquid phase.

The segregation coefficient of Cu in aluminum, $k = C_{Al} / C_{bulk}$, was derived from the μ-XRF map in Fig. C.2.1b as *at least* (1-2)×10^3.

Despite the high segregation coefficient in Al, not all metal clusters can be removed by gettering of solar cell materials. Figure C.2.3 shows an example of results obtained on as-grown Astropower sheet material which was subject to a backside aluminum gettering sequence for 4 hrs at 800°C. A coarse XBIC scan over the front surface reveals two prominent features of low minority carrier diffusion length that have persisted despite the Al gettering treatment: (a) strongly recombination-active grain boundaries, appearing as dark lines, and (b) localized intragranular defects, appearing as dark dots within the grains.

μ-XRF point spectra revealed that Fe was present en masse at both these locations, with a small contribution from Cr in the case of certain intragranular defects. It was found from high-resolution μ-XRF maps that the intragranular defects are irregular in shape and consist of an agglomeration of many nanoparticles, as shown in Figs. C.2.4a and C.2.4b. The grain boundaries were also decorated by Fe-rich nanoparticles, as shown in Fig. C.2.4c. The chemical states of these particles were measured by μ-XAS; by comparison with standard material, it was deduced that Fe was in the form of iron silicide, as shown in Fig. C.2.4d. The spacing and average size of the iron silicide precipitates along the grain boundaries of this material were significantly homogeneous. The particle density along the surface of the grain boundary was determined to be within the range of $(1\text{-}2)\times10^{7}$ cm^{-2}. The average iron content of each of these precipitates at the grain boundaries was determined to be $(0.69\text{-}2.1)\times10^{6}$ Fe atoms; if these precipitates assumed to be spherical, they would have radii of approximately 23±5 nm.

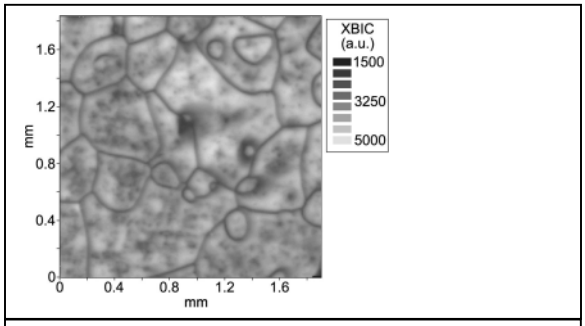

Fig. C.2.3. XBIC map of a typical region of Al-gettered sheet material. Features of interest include recombination active grain boundaries and point-like intragranular defects. Dark regions in the map correspond to the areas with high recombination activity.

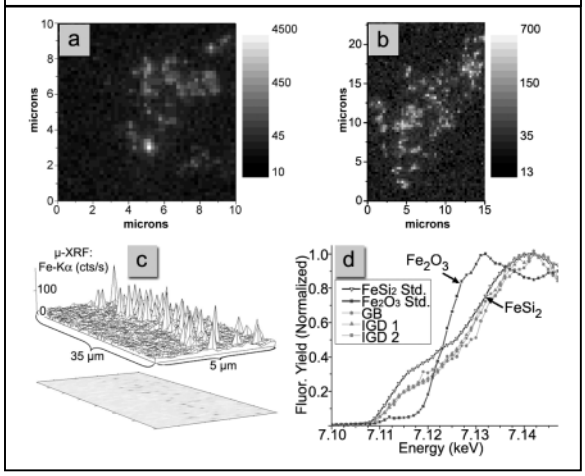

Fig. C.2.4. (a, b) μ-XRF maps of the Fe distribution within typical intragranular defects in sheet material, noted by points of lower XBIC signal in Fig. C.2.3. These defects consist of irregularly-shaped, micron-sized clusters of Fe nanoparticles, and make the largest contribution to the total metal content in this sample. (c) μ-XRF map of Fe nanoparticles within a typical grain boundary, shown in 3D (above) and in 2D projection (below). Although each Fe nanoparticle at the grain boundary is only ~23±5 nm in radius, these nanoparticles are also believed to contain a sizeable fraction of the total Fe in this sample, due to their high spatial density. (d) The chemical state of the Fe particles shown in (a-c) is revealed by μ-XAS to be most similar to $FeSi_2$.

There are four possible explanations to the question why some metal clusters cannot be removed by gettering.

The first one is a high binding energy of metals in clusters of metal-oxides or metal-silicates [S.A. McHugo et al., *Physica B* **273-274**, 371 (1999)]). Our data presented in Section C.4 of this report confirmed that such precipitates were observed in some types of mc-Si. However, the numerical majority of precipitates found in our experiments in mc-Si wafers both before and after gettering were metal-silicides.

The second mechanism, suggested by Plekhanov and Tan [P.S. Plekhanov et al., *J. Appl. Phys.* **86**, 2453 (1999)], is kinetically limited precipitate dissolution, which is observed when metal solubility at the gettering temperature is much lower than the total metal concentration in the sample. This mechanism implies that the precipitates can be gettered, but it may take many hours.

The third mechanism is stabilization of metal clusters either by lattice strains of structural defects [R. C. Dorward and J. S. Kirkaldy, J. Mater. Sci. **3**, 502 (1968); M. Kittler and W. Seifert, Solid State Phenom. **95-96**, 197 (2004)] or due to limited diffusivity of silicon self-interstitials which are needed to counterbalance the volumetric shrinkage associated with the dissolving Cu_3Si precipitates [S.A.McHugo et al., J.Appl.Phys. **91**, 6396 (2002); N.Li et al., 14-th NREL workshop (Winter Park, CO, 2004), p.238].

Finally, the fourth possible mechanism is the limited capacity of the gettering layer. With the estimated segregation coefficient $k = 2\times10^3$ and typical solar cell parameters for wafer thickness $d = 240$ μm and Al layer thickness $w = 1$ μm, one can use the following equation:

$$\frac{\text{[Cu] in Bulk After Gettering}}{\text{[Cu] in Bulk Before Gettering}} \equiv \frac{c_{\text{bulk}}}{c_{\text{o}}} = \frac{c_{\text{bulk}}}{\left(\frac{c_{\text{bulk}} \cdot d + c_{\text{Al}} \cdot w}{d}\right)} = \frac{1}{1+\frac{k \cdot w}{d}}$$

to predict that an upper limit of about 90% of the total metal content can be gettered from the bulk by segregation to the Al layer with $k=10^3$.

While all four mechanisms can play a role in limiting the efficiency of gettering of mc-Si, our experimental data suggest that main contributions are due to the fourth, second, and third mechanisms.

C.3. Role of metal impurities in the formation of shunts (*phase 1, task 4*).

Shunts were analyzed in two types of solar cells, cast and RGS. The samples were pre-characterized with lock-in thermography and LBIC. The areas of interest for μ-XRF analyses were found by in-situ XBIC by correlating LBIC and XBIC maps. Upon a μ-XRF analysis at the shunt location (shown as a small black box in Figs. C.3.1a,b,c), high concentrations of silver (Fig. C.3.1d) and titanium (Fig. C.3.1e) were detected. These metals are used to form the contact fingers of the metallization grid. Despite being found at the shunt location a millimeter away from the nearest contact finger, these metals were present in nearly the same proportions as in the contact strips themselves, which are visible in the lower part of Figures C.3.1d and C.3.1e.

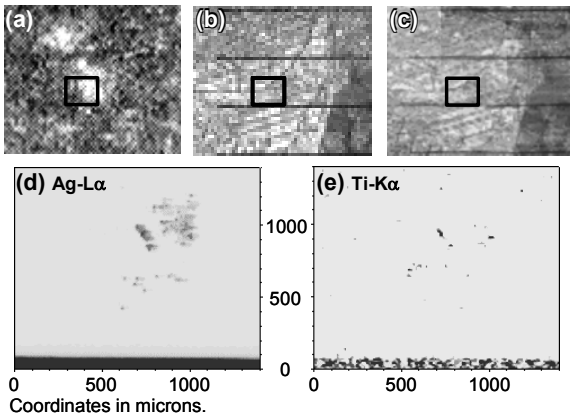

Fig. C.3.1. The procedure followed to determine the presence of metals at a shunting location in a fully-processed cast multicrystalline solar cell: A lock-in thermography map (a) of a 7×9 mm^2 region of the solar cell containing two shunts is correlated with LBIC (b). At the synchrotron, an XBIC map (c) is made over the same region. X-ray fluorescence microscopy (d & e) is performed on the small sub-region containing one shunt (denoted by the box in a, b, and c). Silver (d) and titanium (e) appear in quantities comparable to their concentrations in the contact strips (visible at the bottom of the μ-XRF maps). Residues of the contact metallization are likely the cause of this shunt.

These facts indicate that this shunt is most likely a process-induced defect that was formed during metallization grid deposition, which may form if silver or palladium is deposited directly on the surface of the wafer without a properly-placed titanium buffer layer, or in an event of overfiring. Such a process-induced defect, while not material-specific, can be especially deleterious for solar cells with shallow emitters.

The second group of experiments was performed on RGS material containing current collecting channels. These channels are unique to RGS material and are known, when present in high concentration, to have detrimental effect (lower fill-factor and open-circuit voltage) similar to shunting. The current collecting channels, observed in LBIC with large light penetration depth and as heat-generating spots in thermography maps (see Fig. C.3.2), were found in XBIC maps and analyzed with μ-XRF. As shown in Fig. C.3.3, copper and iron were found to be present at the current collecting channel (bounded between the dashed lines). Lower bounds for the peak metal concentrations (measured in the units of metal atoms per cm^2 of the sample surface) were determined to be 1.7×10^{14} cm^{-2} for Fe and 1.5×10^{14} cm^{-2} for Cu, by assuming the metals lie very near to the wafer surface. The width of the iron peak is close to the diameter of the incident x-ray beam, which indicates that iron formed precipitates localized within a diameter equal to or smaller than the beam size. The copper peak is much broader than the iron peak, indicating that copper more likely forms a colony of small precipitates that appear to decorate an extended defect.

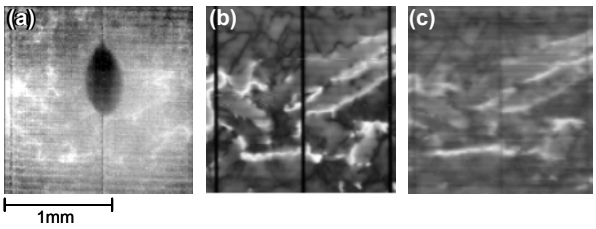

Fig. C.3.2. Detail of a shunt area in an RGS sample. The features evident in the 54 Hz lock-in thermography image taken at 0.52V forward bias (a) resemble those of the 980 nm LBIC (b) and XBIC (c) maps of this area taken at zero bias, indicating that the shunting current is generated at or near the current collecting channels. The oval marker evident in (a) was placed on the surface of the solar cell to mark the region of interest.

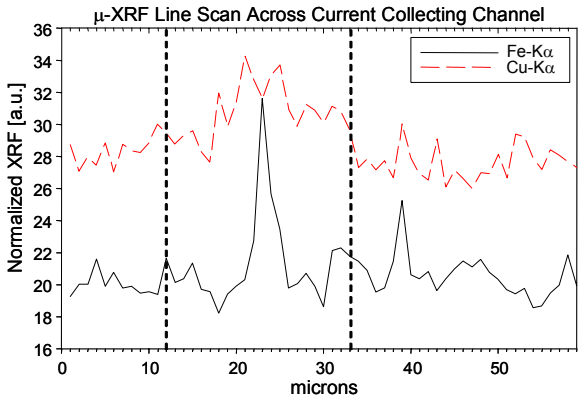

Fig. C.3.3. An x-ray fluorescence microscopy line scan reveals an increase of copper and iron concentrations at a current collecting channel (between vertical dashed lines, identified by XBIC). A lower bound for the peak Fe concentration is 1.7×10^{14} cm^{-2}, and Cu 1.5×10^{14} cm^{-2}. This result suggests that current collecting channels are effective gettering sites for transition metals, which may play a role in shunt formation.

C.4. Chemical nature of metal precipitates formed after heat treatments and interaction of metals with lattice defects and oxygen (*phase 2, tasks 1 and 3*).

Chemical state of iron and copper clusters was studied in a variety of materials to determine whether these metals form gettering-resistant chemical compounds, such as oxides and silicates.

Copper-rich clusters were studied in four types of silicon materials with varying amounts of oxygen: ("sample 1") Float zone silicon intentionally contaminated with (3-4)×10^{16} Cu/cm^{-3} during crystal growth; ("sample 2") Misfit dislocation heterostructure, consisting of a 2 μm thick n-type $Si_{0.98}Ge_{0.02}$ middle layer between a 2.5 μm n-type silicon bottom buffer layer on a (001) silicon substrate and a 2.5 μm thick n-type silicon cap layer, intentionally contaminated with Cu at 800°C; ("sample 3") Czochralski silicon containing approximately 1.8×10^{6} cm^{-3} oxygen precipitates and approximately 1.5×10^{15} cm^{-3} boron intentionally contaminated with Cu at 1200°C; ("sample 4") As-grown, cast mc-Si wafer extracted from near the bottom of the cast mc-Si ingot, where the interstitial oxygen concentration can be as high as 10^{18} cm^{-3}. Prior to μ-XAS analyses, each Si sample was mapped with μ-XRF to reveal the precise distribution of Cu-rich clusters.

Cu K-edge μ-XANES scans of the copper-rich clusters in all four samples yielded strikingly similar spectra to Cu_3Si standard material (Fig. C.4.1). No indications of Cu clusters in chemical state other than copper-silicide was found in these samples.

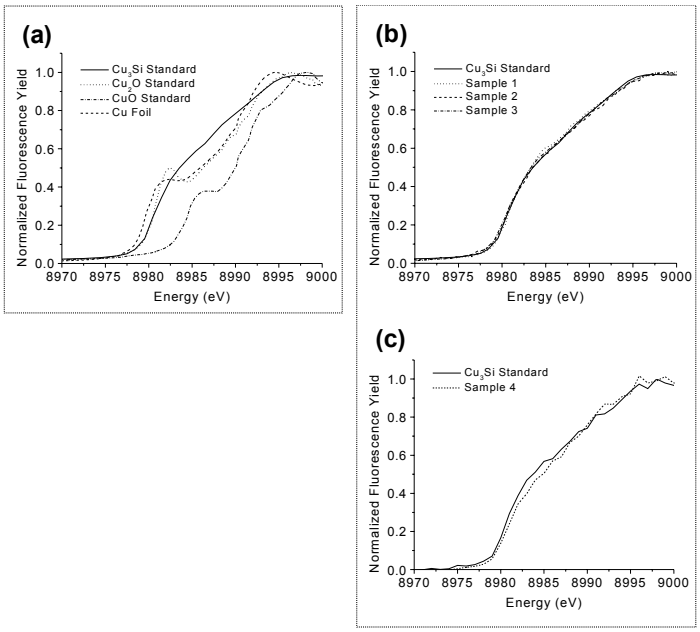

Fig. C.4.1. μ-XANES showing the spectra of standard materials (a), and then the excellent match of Cu-rich clusters in a variety of silicon materials with the Cu_3Si standard (b,c, taken at different beamlines).

Iron-rich clusters were characterized in as-grown and processed cast mc-Si. XBIC maps revealed certain grain boundaries with exceptionally high recombination activity. Multiple iron-rich clusters were detected by μ-XRF at these locations, as the maps in Fig. C.4.2 and Fig. C.4.3 demonstrate. These iron-rich clusters populating grain boundaries can be divided into two distinct types, with distinct physical properties. Firstly, while the vast majority of iron-rich clusters are small (e.g. P1, P3, and P4 in Fig. C.4.2b, and all particles in Fig. C.4.3b), some rare clusters

have nearly two orders of magnitude higher μ-XRF Fe counts (e.g. P2 in Fig. C.4.2b; note the log scale of Fe concentration). An analysis by μ-XAS reveals that the clusters with smaller Fe counts are composed of iron-silicide ($FeSi_2$), while the clusters with much larger Fe counts are composed of oxidized iron (Fe_2O_3), as shown in Fig. C.4.4a and C.4.4b, respectively.

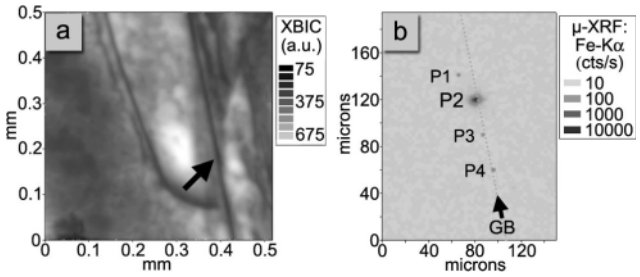

Fig. C.4.2. (a) Typical XBIC image of a cast mc-Si sample. The arrow in (a) points to a recombination-active grain boundary, a region of which was analyzed by μ-XRF in (b). Fe-rich clusters are found along the grain boundary, highlighted by the arrow and the dotted line in (b). Note the log scale of μ-XRF Fe-Kα signal intensity, indicating that P2 has approximately two orders of magnitude higher counts than the others.

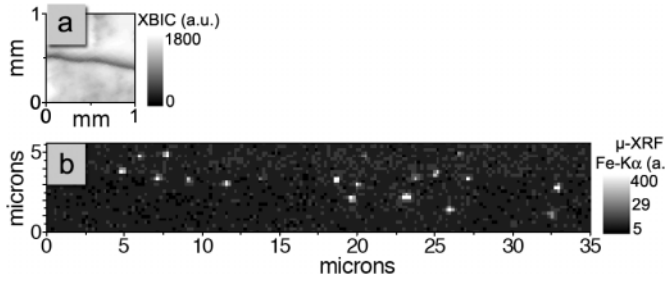

Fig. C.4.3. (a) Large area XBIC and (b) high-resolution μ-XRF map of the iron distribution at a grain boundary in as-grown cast mc-Si. Several $FeSi_2$ nanoprecipitates are observed. Although some clustering is evident on a micron-scale, on a larger scale these $FeSi_2$ nanoprecipitates are distributed rather homogeneously.

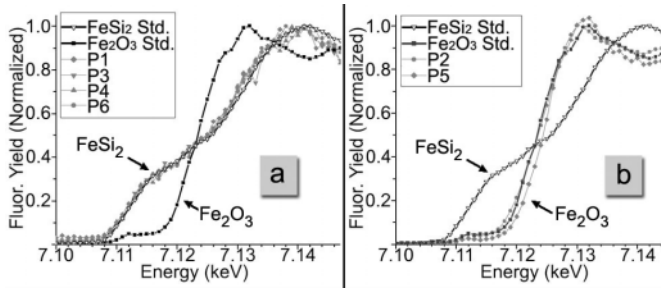

Fig. C.4.4. μ-XAS data discern two types of Fe-rich cluster in cast mc-Si material: (a) smaller iron silicide ($FeSi_2$) and (b) larger iron oxide (Fe_2O_3). Data labels correspond to precipitates viewed in the μ-XRF image Fig. C.4.2.

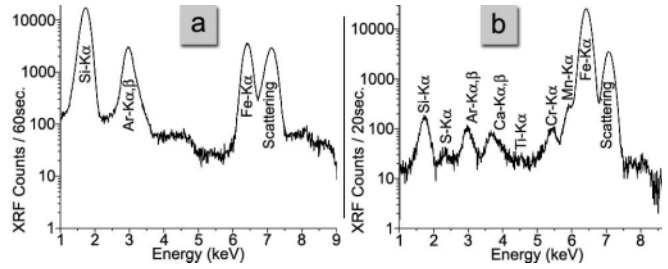

Fig. C.4.5. Typical μ-XRF point scans for the two types of Fe-rich clusters in cast mc-Si: (a) Smaller $FeSi_2$ clusters, without detectable quantities of other metals, and (b) larger Fe_2O_3 particles, wherein iron is accompanied by other elements reminiscent of ceramics, dirt, and stainless steel.

The compositions of these clusters also differ, as determined by the μ-XRF point scans. While the Fe_2O_3 clusters typically show appreciable amounts of other contaminants such as Cr, Mn, and Ca (Fig. C.4.5b), the smaller $FeSi_2$ clusters generally show none of these above the μ-XRF detection limit (Fig C.4.5a). Only in as-grown material can Ni and Cu be found precipitated in the immediate vicinity of $FeSi_2$ in detectable quantities, but not Cr, Mn, Ti, or Ca.

Additionally, the morphologies and orientations of these two types of cluster are very distinct. The large Fe_2O_3 clusters do not appear to be preferentially oriented along the grain boundary or the crystal growth direction. In contrast, the $FeSi_2$ particles are elongated along the grain boundary only in the direction of crystal growth, by a factor of at least 3-4.

The distributions of these clusters also differ. While the large Fe_2O_3 clusters are inhomogeneously distributed, the smaller $FeSi_2$ clusters appear to be more regularly spaced. Taking into account the attenuation length of the Fe-Kα fluorescence in Si, one calculates a $FeSi_2$ precipitate density of $(1.5\text{-}2)\times10^6$ per cm^2 of grain boundary surface area in Fig. C.4.3, resulting in an average spacing between precipitates of 7-8 μm along the grain boundary.

In the past, it has been suggested that oxidized metallic precipitates may form within silicon because many species of metal atom, e.g. Cu and Fe, have higher binding energies to oxidized compounds such as silicates and oxides than to silicides [see, e.g., S.A. McHugo et al., J.Appl.Physics **89**, 4282 (2001)*;* S.A.McHugo et al., J.Appl.Phys. **91**, 6396 (2002)]. While it is true that metals bond strongly to oxygen, the same can also be said for silicon, and thus an analysis of whether a metallic oxide, silicate, or silicide will form should take this competitive oxidation potential into consideration. It is known that oxygen can form a very stable and electrically inactive interstitial complex with silicon (O_i), not to mention SiO_2. Table V reproduces the *enthalpy of formation per oxygen atom* (the figure of merit in a balanced equation) from individual elements for a selection of oxidized species, demonstrating that when [Si] >> [O] > [Cu], equilibrium thermodynamics predicts that silicon will be the predominant oxidized species.

While the precise values of enthalpies of formation cited in Table V do not reflect the additional detailed calculations necessary to account for the formation of a species within a silicon lattice, Table V indicates that in the presence of silicon, a strong competitor for oxygen, Cu and Fe will likely be reduced or remain unoxidized. Based on these observations and our μ-XAS measurements, it is concluded that both Cu and Fe in the presence of Si with [O] << [Si] will not tend to form stable chemical bonds with oxygen, and thus will likely either form non-oxidized precipitates, out-diffuse, or remain dissolved if solubility permits.

Table V. The enthalpies of formation per mol per oxygen atom at 298.15K for various oxidized metal species. It is shown that the binding energy of oxygen to silicon is far greater than that of oxygen to iron or to copper. The same is not true for all metals, e.g. hafnium. Data are from *CRC Handbook of Chemistry and Physics, 84th Edition* (CRC Press, 2003).

Compound	$\Delta_f H°$ (kJ/mol)
1/2 HfO_2	-572.4
1/2 ZrO_2	-550.3
1/2 TiO_2	-472.0
1/2 SiO_2	**-455.4**
1/4 Fe_2SiO_4	-370.0
1/4 Fe_3O_4	-279.6
1/3 Fe_2O_3	-274.7
Cu_2O	-168.6
CuO	-157.3

C.5. Recombination activity and thermal stability of complexes which metals form in mc-Si (*phase 2, task 2*).

In the course of our research, we had numerous confirmations of high recombination activity of metal clusters in mc-Si. For example, Fig. C.5.1 gives an example how μ-XRF maps, characteristic of metal distribution in solar cells, correlate with XBIC maps, characteristic of minority carrier diffusion length.

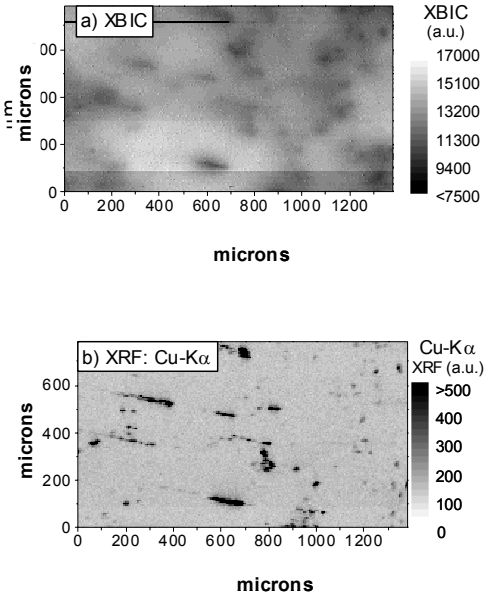

Fig. C.5.1. (a) x-ray beam induced current and (b) Cu-Kα x-ray fluorescence microscopy maps of float zone silicon contaminated with (3-4)×10^{16} Cu cm^{-3} during crystal growth. Notice the strong correlation between the presence of copper-rich clusters (b) and the decrease of current collection efficiency (a).

The impact of transition metals on cell efficiency is determined by their spatial distribution. This can be understood by considering a hypothetical silicon sample with 10^{14} cm^{-3} iron-boron pairs (Fe_i-B_s) or interstitial iron (Fe_i). The minority carrier diffusion length in such a sample would be approximately 20 μm or 10 μm, respectively [A.A. Istratov et al. Appl. Phys. A **70,** 489 (2000)]. Now, let us assume these iron atoms are allowed to diffuse towards one another and form precipitates of iron-silicide. If we approximate the new minority carrier diffusion length as the distance between neighboring iron silicide clusters, then, if the same amount of iron forms precipitates with diameters of 60 nm, the diffusion length would be ~30 μm; if precipitates with diameters 350 nm form, the average diffusion length would be ~180 μm, etc. One can quickly see the pattern: with increasing average precipitate size (and decreasing density of precipitates), the minority carrier diffusion length increases. It can thus be concluded that it is the distribution of metals, and not their total bulk concentration, that affects the mc-Si cell efficiency.

The iron-rich clusters analyzed in this study can be divided into two distinct groups, larger particles and smaller precipitates. Larger particles (diameter ≥ 1 μm) are present in rather low spatial densities and are believed to be inclusions originating from foreign sources, e.g. the feedstock, growth surfaces, and/or production equipment. These inclusions are (a) accompanied by lesser amounts of other metals such as Cr, Ni, Mn, Ti, S, or Ca, suggestive of stainless steels or ceramics, and/or (b) in an oxidized chemical state. Smaller (dia. < 800 nm, typically < 100 nm) iron silicide precipitates are observed in much higher spatial densities, separated by as little as a few microns. Despite their small size, a large amount of iron (up to $10^{14\text{-}15}$ cm^{-3}) is estimated to be contained in these iron silicide nanoprecipitates due to their high spatial density. Copper was found primarily in small copper-silicide precipitates; no oxidized copper particles was observed.

The smaller, more distributed iron silicide clusters are believed to have a large impact on solar cell device performance, the reason being the small distance separating adjacent clusters. This is substantiated by the correlation between the recombination active grain boundaries observed in numerous XBIC images presented in our quarterly reports, publications, and in this re-

port, and the presence of metal silicide precipitates separated by distances of only a few microns. A model developed by [A. Fedotov et al., J. Cryst. Growth **104,** 186 (1990)] predicts that when the distance separating neighboring recombination-active clusters along a grain boundary is less than the minority carrier diffusion length within the grains, the grain boundary becomes noticeably recombination-active for minority carriers. This model agrees with our observations. Similarly, much lower diffusion lengths were observed in grains which contained higher density of metal clusters at intragranular defects.

Iron-oxide particles are expected to be very stable at typical gettering temperatures, and are extremely difficult to remove. However, due to their low spatial density, they have limited impact on device performance. Smaller metal-silicide particles, usually present in much higher density, have much more serious lifetime limiting effect. Additionally, interstitially and substitutionally dissolved metals, even if present in minute concentration, can greatly impact the solar cell performance. Metal-silicide precipitates are relatively easy to dissolve. However, due to the large total amount of metals found in these precipitates, the kinetics of gettering is limited by the solubility and diffusivity of metals. Since gettering involves dissolution of metal clusters, i.e., a conversion of precipitated metals into potentially even more recombination active interstitial / substitutional metal atoms, incomplete gettering may lead to no observable improvement or even degradation of minority carrier diffusion length.

Partial dissolution of metal-silicide precipitates during short high temperature heat treatments was demonstrated in the following experiment. One sample from a set of sister wafers from near the bottom of a cast mc-Si ingot was subject to a rapid thermal anneal (RTA) at Fraunhofer ISE for emitter diffusion at 1000°C for 20 seconds. The same grain boundary in the processed sample, as well as the as-grown material, was analyzed by μ-XRF. In the as-grown material (Fig. C.5.2a), large iron clusters could be seen at grain boundaries accompanied by denuded zones (Fig. C.5.2c). Also copper and nickel clusters were detected, although in a lower density (not shown). In the sample processed at 1000°C for 20 seconds, neither copper nor nickel could be detected, while the iron clusters contained only 50% their original iron content. The decrease of iron content at the precipitates corresponds with decreasing material performance. XBIC and LBIC maps indicate a large increase of intragranular recombination activity (Fig C.5.2d), as well as the lack of denuded zones around the grain boundaries. The iron, copper, and nickel dissolved from the precipitates are believed to have diffused into the grains at high temperatures, and re-precipitated at structural defects during cooling. The short high-temperature anneal combined with a rapid cooling rate probably exacerbated the delocalized iron precipitation within the grains, and deteriorated the material properties.

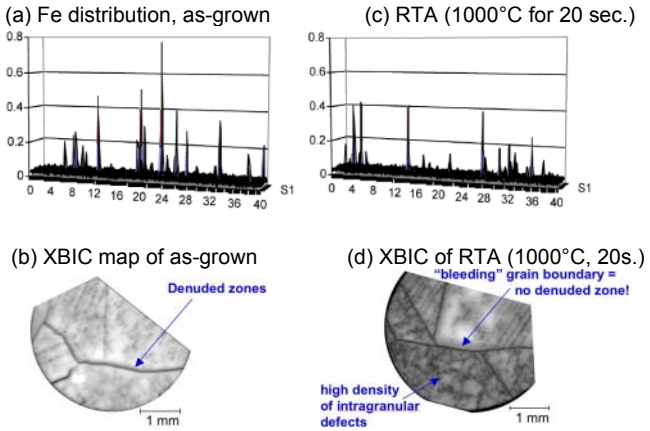

Fig. C.5.2. 40 × 6 μm^2 μ-XRF maps of the iron distribution in grain boundaries of cast mc-Si sister wafers: (a) as-grown and (b) rapid thermal annealed at 1000°C for 20 sec. A comparison of higher resolution μ-XRF maps of numerous precipitates in both samples reveal a 50% reduction in Fe content as a result of high-temperature processing. This dissolved Fe is believed to be responsible for the degradation in minority carrier diffusion length observed in the XBIC images (c and d).

C.6. Pathways of formation of gettering-resistant clusters during mc-Si ingot growth (*phase 3, tasks 1 and 2*).

Experimental evidence obtained in this study enabled us to conclude that the origins of metals in most mc-Si materials include some combination of the following: Metals dissolved in the silicon feedstock, foreign metallic particles introduced with the feedstock, metals originating from furnace or production equipment, and metals diffusing from the walls of the crucible or growth surfaces. Figure C.6.1 is a pictorial representation of the mechanisms of incorporation of metals into solar cells. Each of these mechanisms is discussed briefly below.

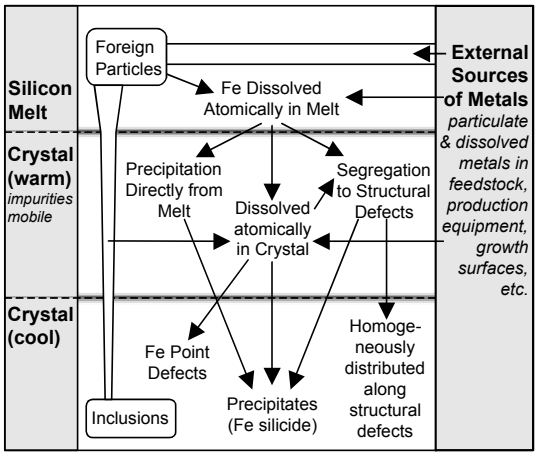

Fig. C.6.1. Graphical representation of the origins of Fe contamination in mc-Si, the physical mechanisms responsible for incorporating large amounts of Fe into the mc-Si material when warm, i.e. temperatures at which impurity atoms are mobile, and the formation mechanisms of the Fe-rich clusters one observes in finished mc-Si material. Two types of Fe-rich cluster are observed in finished material: inclusions of foreign particles introduced into the melt, and iron silicide nanoprecipitates formed from dissolved iron. Note that the partial or complete dissolution of the former can contribute to the formation of the latter.

The hypothesis that foreign particles (originating from the feedstock, production equipment, etc.) are incorporated into the melt is substantiated by the μ-XRF observations of a few metal-rich particles of unusually large sizes (typically ≥ 1 μm). All of these large particles observed have one or both of the following additional characteristics: (a) the coincidence of iron with large amounts of other (often slowly-diffusing) metal species (e.g. Ca, Ti, Cr, Mn, Ni, etc.), the relative proportions of which allude to certain steels or ceramics and (b) an oxidized chemical state. This last point is a significant indicator of foreign particles being included in the melt, as oxidized iron and copper compounds are not thermodynamically favored to form under equilibrium conditions within silicon, as discussed in sec. C.4. However, an Fe_2O_3 particle inserted into the silicon melt should retain its structural integrity for a limited time, as the melting temperature of Fe_2O_3 is approximately 1565°C, about 150°C above the melting temperature of Si. Oxidized Cu particles will dissolve very quickly, as the low melting temperatures of both Cu_2O (1235°C) and CuO (1326°C) is lower than the melting point of silicon (1414°C). Experimental evidence up to this point has shown no evidence for oxidized Cu-rich clusters inside silicon crystals.

The possibility that metals found in cast mc-Si could diffuse from the crucible walls is supported by the fact that iron and other metals are typically present in the silicon nitride crucible lining typically in concentrations as high as parts per million (metal oxides are often added to densify and harden silicon nitride).

As shown in Fig. C.6.1, besides (a) direct incorporation of incompletely dissolved foreign metal-rich particles into the crystal as inclusions, there are several other mechanisms of incorporation of metals into the crystal: (b) direct precipitation of locally supersaturated iron from the

melt (the mechanism suggested in [P.S. Ravishankar et al., J. Crys. Growth **71,** 579 (1985); J. P. Kalejs et al., J. Crystal Growth **109,** 174 (1991)]), (c) segregation of metals dissolved in the melt to structural defects, (d) incorporation of dissolved Fe in the melt into single-crystalline regions of the material as interstitial atoms, and (e) diffusion of Fe from the growth surfaces into the crystal. The latter two mechanisms (d and e) are rather limited in their potential to introduce large amounts of Fe into most mc-Si materials, due to the segregation effect between the melt and the crystal, and to a limited diffusion length of metals within silicon. Mechanism (c) is discussed separately in Section C.7.

The density and size of metal precipitates can be expected to depend on cooling conditions. With slow cooling rates and high metal concentrations, a few "large" (10's of nm dia.) metal silicide precipitates are expected to form. On the other hand, faster cools offer less time for supersaturated metals to diffuse and form large clusters, thus favoring a more homogenous distribution of metals along structural defects, either atomically or as smaller precipitates. This dependence was observed experimentally in our studies: cast mc-Si which is cooled very slowly contained relatively larger particles with larger spacing in between, whereas sheet material, which is grown and cooled comparatively quickly, exhibited precipitates of closer spacing and smaller average size despite a total Fe content 1-2 orders of magnitude higher than cast mc-Si. The distribution of metal clusters between grain boundaries and intragranular defects is likely to depend both on the cooling regime and the availability and type of nucleations sites within grains.

Quantitative analysis of μ-XRF maps allowed us to estimate the total iron concentration in Astropower sheet material as $(0.1\text{-}3)\times10^{16}$ Fe/cm^3 at intragranular defects and $(0.4\text{-}2)\times10^{15}$ Fe/cm^3 at grain boundaries. In cast material, the majority of iron clusters were observed at grain boundaries; the estimated iron concentration in these clusters was $(0.5\text{-}3)\times10^{14}$ Fe/cm^3. Previous NAA analyses on these materials indicate total Fe contents of $(0.87\text{-}1.6)\times10^{16}$ Fe/cm^3 for sheet mc-Si and $(4.0\text{-}4.7)\times10^{14}$ Fe/cm^3 for cast mc-Si. Hence, the amount of Fe contained in these samples in iron silicide nanoprecipitates is comparable to the total amount of Fe in these samples, as measured by NAA. The iron silicide nanoprecipitates – especially those dispersed homogeneously along the grain boundaries – are extremely difficult to detect with most standard analytical techniques, due to their small spatial dimensions and comparatively large distances separating neighboring particles. Yet, it is precisely this form of Fe – homogeneously distributed in smaller clusters – that has a strong negative impact on the device performance.

C.7. Segregation of metals at structural defects (*additional topic, not on the task list; extends phase 3, topic 2 and phase 2, topic 2*).

Simple equilibrium segregation models alone cannot account for the fact that $10^{14\text{-}16}$ cm^{-3} of Fe and other transition metals (Sec. C.1) are present in mc-Si materials. Were the amount of metals incorporated into the final crystal determined simply by their segregation into single-crystalline regions (described by the segregation coefficient (the ratio of Fe solubilities in single crystalline silicon and in the melt) which typically ranges from 10^{-5} to10^{-7} cm^{-3} [S. Mahajan and K. S. S. Harsha, *Principles of Growth and Processing of Semiconductors* (WCB/McGraw-Hill, USA, 1999)]), this would imply that the melt at the solid-liquid interface contained as much as 0.001%-1% of transition metals! If in fact this high metal concentrations were present, instability in the solid-liquid interface would arise, and certainly columnar crystal growth with centimeter-sized grains would not proceed as desired in the case of cast mc-Si.

Incorporation of large oxidized particles could account for a fraction of the total metal content of mc-Si, but according to our estimates this fraction is small.

One of the mechanisms, which in our opinion could play an important role in incorporation of metals in mc-Si, is segregation of metals to structural defects. It is known that the solubility of metals in polysilicon is higher than in single-crystalline silicon [segregation of Cu was studied by R. C. Dorward and J. S. Kirkaldy, J. Mater. Sci. **3,** 502 (1968)], which is a consequence of the interaction of metals with dangling or reconstructed silicon bonds in structural defects (e.g. grain boundaries), as well as the reduction of strain energy from metals settling in a distorted silicon lattice near the structural defects. A higher metal solubility in mc-Si would lead to a lower effective segregation coefficient and incorporation of a higher metal concentration in the mc-Si ingots.

To determine how the solubility of iron in mc-Si differs from that in single-crystalline Si, we used a structure consisting of a thin polysilicon layer deposited on a CZ-grown silicon wafer. The advantage of polysilicon is that it has a high density of grain boundaries which is practically homogeneous on a macroscopic scale, and it can easily be deposited on a CZ substrate which can then be used as in-situ reference. The sample analyzed in Fig C.7.1 consisted of 11 μm of nominally undoped polysilicon deposited on top of a p^- silicon substrate. The sample was contaminated from the backside by scratching with an iron wire, annealed in a vertical furnace at 1150°C in N_2 + 5% H_2 ambient for 90 min, and quenched in silicone oil.

A decrease in the iron concentration in the substrate towards the interface with polysilicon stems from relaxation gettering of iron during the silicone oil quench, whereby supersaturated iron diffuses from the substrate to the polysilicon layer. The total amount of iron that was gettered in the poly-Si layer due to a combination of segregation and relaxation mechanisms can be determined, in the units of Fe atoms per cm^2 of the sample surface, by integrating the area "A" of the plot in Fig. C.7.1a between the SIMS data in polySi and the equilibrium iron solubility. The total amount of iron that diffused into the polysilicon layer during cooling driven by relaxation can be calculated by integrating the area "B" in the substrate. By performing the integration, one obtains $A=1.44\times10^{13}$ cm^{-2} and $B=2.52\times10^{12}$ cm^{-2}. Since the area A is 6.4 times greater than the area B, relaxation gettering alone cannot account for all iron accumulated in concentration above its equilibrium solubility in the area B. The segregation coefficient k can be determined as follows: $k= S(poly)/S(substrate) = (Fe_{eq}+(A-B)/d)/Fe_{eq} \approx 2.6$, where Fe_{eq} is the equilibrium Fe solubility in silicon at the diffusion temperature, d is the thickness of the poly-Si layer,

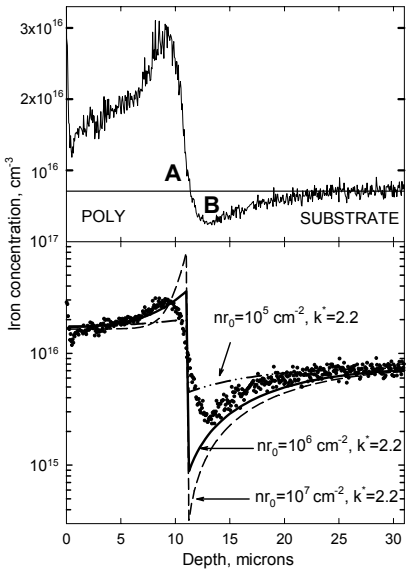

Fig. C.7.1. Secondary ion mass spectroscopy depth profile of iron diffused in 11 μm polySi/Si structure at 1150°C and quenched in silicone oil. (a) depth profile plotted using a linear concentration scale. The solid horizontal line is the equilibrium iron solubility at the diffusion temperature. (b) The same depth profile plotted on a logarithmical scale together with the results of numerical modeling. The solid line represents the best fit, the dashed lines are variations of the nr_0 product.

and *S(poly)* and *S(substrate)* are the solubilities of iron in polysilicon and in the substrate. A similar value (k=2.2) was obtained from computer modeling of gettering of iron during cooling.

Another experiment was performed with 1.1 microns thick polysilicon layer, which was quenched in 10% NaOH after anneal at 1100°C. In this case, no visible transient in iron concentration in the substrate was observed, and the segregation coefficient extracted from the ratio of iron concentrations in the substrate and in the poly was approximately 4. An experiment with a different structure (370 nm poly-Si on 197 nm SiO_2 on Si substrate) yielded $k \approx 16$ at 1020°C. It is important to note that polysilicon (and to even greater extent multicrystalline silicon) is very inhomogeneous and contains both grain boundaries with significant lattice strain which segregate the impurities and relatively unstressed silicon within the grains which has no segregation effect. Hence, the macroscopic segregation coefficient observed in the experiments should depend not only on the microscopic structure of grain boundaries (such as misorientation of the grains forming the boundary), but also on the grain size and could vary depending on the thickness and growth conditions of the layer.

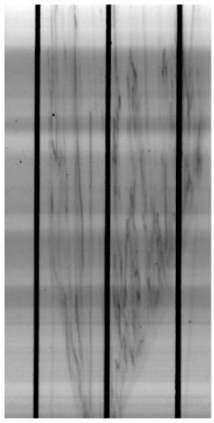

Fig. C.7.2. LBIC map of a 2x1 cm^2 region in a Evergreen string ribbon solar cell.

The amount of segregation of Cu in multicrystalline silicon observed by Dorward and Kirkaldy was very substantial at low temperatures, around 3 orders of magnitude at 700°C, and dropped to a factor of two or less at temperatures above 900°C. Our studies of segregation of iron in polysilicon were performed at high temperatures, over 1000°C, and resulted in segregation coefficients from 2.6 to 16 which are similar or higher than the values observed by Dorward and Kirkaldy for copper in the same range of temperatures.

It is instructive to make a simple estimate of the capacity of grain boundaries. The sample mapped by LBIC in Fig. C.7.2 is 2 by 1 cm in size, 0.25 mm thick. We counted 40 grain boundaries within this sample, the average length of each boundary is 1.7 cm. The total area of all boundaries can be estimated as 1.7 cm^2, or 0.85 cm^2 per cm^2 of the surface area. If the metal density at the boundaries is 1 metal atom per 500 silicon atoms, the segregated Fe concentration will be 8.5×10^{11} cm^{-2} areal density, or 3.4×10^{13} cm^{-3} volume density.

C.8. Impact of the cooling rate on metal distribution in mc-Si (*not on the task list, expands phase 2, topic 1, and phase 3, topic 2*)

For this study, samples of mc-Si were intentionally contaminated with Fe, Cu, and Ni. "Slowly cooled" samples were cooled to room temperature inside of the furnace. "Quenched/re-annealed" samples were quenched in silicone oil, etched to remove surface metal-silicides, inserted into a preheated furnace running at 655°C, annealed for 2.5 hours, and then slowly cooled in the furnace within approximately 12 hours. In the slowly cooled mc-Si samples (see our article in the August 2004 NREL workshop proceedings for details) Cu and Ni formed just a few localized precipitates along the grain boundaries and oxygen precipitates. Despite its higher solubility, copper formed lower density of precipitates than nickel, which agrees with a higher barrier for precipitation of Cu than of Ni.

The precipitation behavior of Cu and Ni in "quenched /reannealed" samples was found to be completely different. In mc-Si (Fig. C.8.1) all grain boundaries and dislocations were evenly decorated. Once the samples were inserted back into preheated furnace running at 655^{o}C, quenched-in metals got mobile and at the same time remained highly supersaturated. Supersaturation of metals determines the energy gained by a metal when it precipitates and therefore the height of potential barrier for precipitation which it can overcome. In such conditions metals can precipitate at sites which would be unfavorable at lower supersaturation levels, when the driving force for precipitation is low.

These observations confirm that faster cooling of ribbon/sheet/ingot is likely to lead to a higher density of small metal precipitates. Slow cooling would stimulate formation of a lower density of larger metal precipitates, which are likely to affect the minority carrier diffusion length to a lesser extent than high density of small precipitates. These results suggest that it might be possible to engineer the distribution of metals in an mc-Si wafer by a properly designed heat treatment.

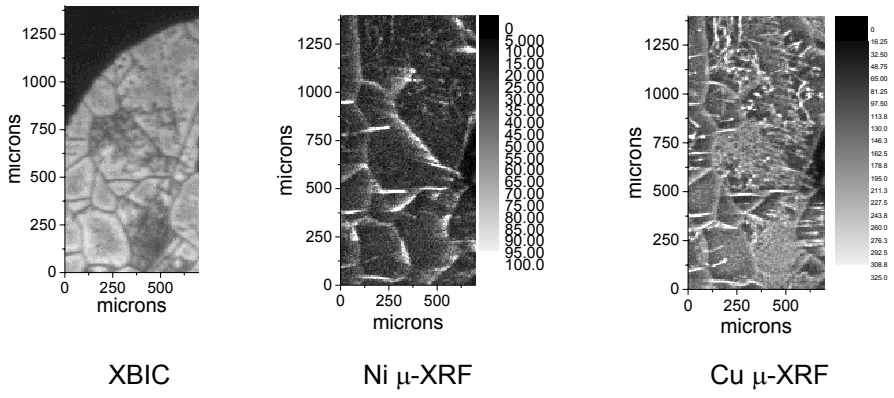

Fig. C.8.1. XBIC, nickel μ-XRF, and copper μ-XRF maps of mc-FZ samples which were intentionally contaminated at 1200^{0}C, quenched and re-annealed at 655^{o}C.

C.9. Differences and similarities between metal clusters in mc-Si materials from different manufacturers (*not on the task list, expands phase 2, topic 1, and phase 3, topic 2*).

Cast, sheet, ribbon, and mc-FZ materials were compared in terms of distribution of metal clusters to determine the features which are common to all these materials and to identify the differences, specific to a particular material.

Similarities: Metals in all samples exhibited a tendency to precipitate at structural defects, especially two-dimensional defect surfaces such as grain boundaries. In certain materials, metals were also concentrated at intragranular locations, presumably associated with structural defects. Often several metals (e.g., Fe and Cu) were found to precipitate at the same location (within the limits of the spatial resolution of the technique, which varies between 200 nm and 2 μm, depending on the beamline used).

The large majority of metal-rich clusters observed in all materials were in a metal-silicide chemical state. Only very few large metal clusters were oxidized. Those particles, judging from their elemental composition and size, appear to be introduced into the melt from a foreign source (such as impurity particles in the feedstock), and before fully dissolving, they are incorporated into the final silicon crystal as inclusions. Dissolved metals from these particles are likely to be the source of the smaller and more distributed metal-silicide nanoparticles observed at grain boundaries and in intragranular defect clusters in sheet material.

Differences: the most significant differences between the different types of materials were in the size and spatial distribution of metal-rich precipitates. For example, micron-sized clusters of metal-rich particles are found at intragranular locations in sheet material, while only isolated intragranular metal-rich nanoparticles have been observed in cast material. In addition, the sizes and distances of metal-rich particles at grain boundaries in as-grown cast mc-Si and sheet material differs as well. In a sheet material sample scanned with high-resolution μ-XRF, iron silicide particles roughly 23 nm in radius are separated by 2-3 μm, while in a cast mc-Si sample, these particles were roughly 30 nm in radius and separated by 8-9 μm. In other words, metal-rich particles may be larger in average size and spaced by larger distances, or smaller in size and closer together. These distributions are material-specific.

There are also differences in distribution observed within the same material, e.g. cast mc-Si. Whereas at the bottom of the ingot relatively larger and more isolated Cu- and Ni-rich clusters were observed at a grain boundary, smaller and more homogeneously distributed clusters were found at the top of the ingot. This could be due to differences in the cooling rates of the two areas of the ingot.

It is known that the metal distribution in mc-Si can be affected by a combination of one or more of the following factors: (a) feedstock impurity content, (b) crucible and crucible lining impurity content, (c) contamination by foreign particles during growth, and (d) growth parameters. Variations between different materials analyzed in this study are believed to be due to one or more of these factors. Variations are even expected from run to run within one type of material, as parameters such as the feedstock impurity content may vary. As this affects the final solar cell device performance, strict control of all variables is required to meet production quality standards.

D. Summary and Relevance to the photovoltaic community

Average metal content of solar cells. Neutron activation analysis was performed to determine the total metal content of solar-grade multicrystalline silicon. The dominant metal impurities were found to be Fe (6×10^{14} cm^{-3} to 1.5×10^{16} cm^{-3}, depending on the material), Ni (up to 1.8×10^{15} cm^{-3}), Co (1.7×10^{12} cm^{-3} to 9.7×10^{13} cm^{-3}), Mo (6.4×10^{12} cm^{-3} to 4.6×10^{13} cm^{-3}), and Cr (1.7×10^{12} cm^{-3} to 1.8×10^{15} cm^{-3}). Copper was also detected (less than 2.4×10^{14} cm^{-3}), but its concentration could not be accurately determined because of a very short decay time of the corresponding radioactive isotope. The total metal concentration of the wafers would be sufficient to decrease the average minority carrier diffusing length to several microns or less, if all metals were in the interstitial or substitutional state.

Metal content of good and bad regions. No systematic differences were found between the metal content of "good" and "bad" regions, except for a consistently higher gold concentration in "bad" regions. Some metals were even found in slightly higher concentration in the "good" regions than in the "bad" regions. This implies that the "good" and "bad" regions differ not by the amount of metals, but by their spatial distribution and by the recombination activity of clusters and point defects which these metals form.

Shunts and transition metals. We demonstrated that transition metal contamination is one of possible mechanisms of shunt formation. We observed precipitates of Ag and Ti at a shunt location in cast mc-Si cell, which indicated a possibility of process-induced shunt. Clusters of iron and copper were found near the current-collecting channels in RGS material. These channels are unique to RGS material grown under certain conditions and are known to have detrimental effect (lower fill-factor and open-circuit voltage) similar to shunting.

Chemical state and distribution of iron clusters in mc-Si. The iron-rich clusters analyzed in this study can be divided into two distinct groups: 1) Larger particles (diameter $\geq$ 1 μm) which are present in rather low spatial densities and are believed to be inclusions originating from foreign sources, e.g. the feedstock, growth surfaces, and/or production equipment. These inclusions are (a) accompanied by lesser amounts of other metals such as Cr, Ni, Mn, Ti, S, or Ca, suggestive of stainless steels or ceramics, and/or (b) in an oxidized chemical state, both indicators of foreign origins. 2) Smaller (dia. < 800 nm, typically < 100 nm) iron silicide precipitates, observed in much higher spatial densities and separated by as little as a few microns. Despite their small size, a large amount of iron (up to $10^{14\text{-}15}$ cm^{-3}) is estimated to be contained in these iron silicide nanoprecipitates, due to their homogeneous distribution and high spatial density along structural defects.

Chemical state and distribution of copper clusters in mc-Si. All Cu clusters observed in our experiments were copper-silicide; no copper-oxide or copper-silicate particles were observed. Copper was shown to precipitate predominantly at extended defects such as grain boundaries and dislocations. The distribution of copper depends on the cooling rate (i.e., on the Cu supersaturation level).

Interaction of metals with oxygen and formation of gettering-resistant clusters. Thermodynamic considerations indicate that metals are unlikely to form complexes with oxygen dissolved in sili-

con wafers because the binding energy of oxygen to silicon is greater than that of oxygen to most transition metals. Particles in which metals were found in oxidized state were found in very low density and were concluded to be incompletely dissolved inclusions trapped from the melt.

Segregation of metals at grain boundaries and structural defects. We obtained experimental evidence that iron aggregates at structural defects due to a combination of relaxation and segregation mechanisms. Similar effect has been earlier reported for copper. Segregation at grain boundaries and dislocations is likely to be one of the mechanisms of incorporation of high metal concentrations in mc-Si ingots from the melt.

Sources and pathways of metal contamination in solar cell materials. The chemical and elemental composition of large metal-rich clusters in mc-Si suggests that metal contamination originates from metal-rich particles or dissolved metals in the growth surfaces, feedstock, and/or production equipment. Large amounts of metals can be incorporated into mc-Si primarily via three mechanisms: (a) the inclusion of incompletely dissolved foreign metal-rich particles, (b) the direct precipitation of locally supersaturated metal at the solid-liquid interface in the vicinity of structural defects, and (c) the segregation of metals to structural defects. Once inside the crystal at elevated but decreasing temperatures, dissolved metals can form metal-silicide nanoprecipitates.

Gettering of metals in solar cells. We demonstrated that short heat treatments may partially dissolve metal clusters and lead to a minority carrier diffusion length degradation within the grains. The majority of metal clusters observed in our studies are in the state of metal silicide which is relatively easy to dissolve. As suggested by Plekhanov and Tan, gettering may take a long time if metal solubility at the gettering temperature is much less than the total metal content of the wafer. Segregation coefficient of Cu in Al was found to be greater or equal than S(Cu in Al)/S(Cu in Si)= 2×10^3. The difficulties with gettering of metals in mc-Si appear to be primarily due to high metal content of mc-Si and limited capacity of the gettering layers. Due to the limited capacity of a standard 1-2 microns thick Al layer, only 90% to 95% of Cu can be removed from a solar cell. Incomplete gettering may result in no visible improvement in minority carrier diffusion length.

Impact of the cooling rate. Our data indicate that cooling rate has a significant impact on precipitation behavior of Cu and Ni: they can either very selectively precipitate at certain locations at grain boundaries and oxygen precipitates, or evenly decorate all boundaries and dislocations. This implies that properly chosen heat treatments can be used to engineer the distribution of metal clusters in the samples.

Analysis of metal clusters in a wide variety of mc-Si materials. It was confirmed that while the density and spatial distribution of metal clusters depends on the feedstock quality and growth conditions, the chemical state and general trends in distribution of metal clusters are similar for all mc-Si materials.

Possible practical solutions for decreasing impact of metals on solar cells. Solar cells can tolerate much higher amounts of precipitated metals compared to interstitially/substitutionally dissolved metals in the lattice. The recombination properties of metals vary depending on their chemical or structural state and spatial distribution. The total metal content of mc-Si materials is typically so

high that it is not feasible, due to the kinetic constraints and limited gettering layer capacity, to remove all these metals by gettering within a temperature cycle compatible with solar cell production cycle. One the other hand, instead of removing the metals from the cells it is sufficient to convert them to a less recombination efficient state. This approach can be called metal passivation through defect engineering.

E. Acknowledgements.

This study would not be possible without fruitful collaboration with our colleagues from NREL (T. F. Ciszek, R. Mcconnell, R. Matson, B. Sopori), Fraunhofer ISE (C. Ballif, S. Peters, J. Isenberg, W. Warta, S. Riepe, M. Rinio, S. Rein, S. Glunz, and R. Schindler), Georgia Tech (A. Upadhyaya, M.Sheoran, A.Rohatgi), University of Konstanz (G. Hahn), Max Planck Institute for Microstructure Physics in Halle (O. Breitenstein, J.-P. Rakotoniaina), University of Leipzig (M. Heuer), BP Solar (D. W. Cunningham), Evergreen Solar (A. Gabor), GE Energy (formerly Astropower) (R. Jonczyk), RWE Schott Solar (J. Kalejs), Sumitomo Mitsibushi Silicon (W.Huber) as well as staff scientists from the Advanced Light Source (M. A. Marcus, A. C. Thompson), Advanced Photon Source (B. Lai, Z. Cai), and LBNL Nuclear Physics Division (R. J. Mcdonald and A. R. Smith). Contributions of O. F. Vyvenko, H. Hieslmair, and S. A. McHugo were instrumental for development of experimental approaches used in this study and for determining the directions of research. Last but not least we would like to thank D. Macdonald and A. Cuevas (Australian National University), S. K. Estreicher (Texas Tech), W. Schröter (University of Göttingen), O.Breitenstein (MPI Halle), and our present and past group members, M. Pickett, P. Zhang, H. Väinölä, S.A. McHugo, and D. Schleuning, for numerous discussions. T. Buonassisi would like to thank the DAAD for a summer 2004 scholarship which supported his trip to Germany to discuss with work with our German colleagues. The operations of the Advanced Light Source at Lawrence Berkeley National Laboratory are supported by the Director, Office of Science, Office of Basic Energy Sciences, Materials Sciences Division, of the US Department of Energy under Contract No. DEAC03-76SF00098. Use of the Advanced Photon Source was supported by the US Department of Energy, Office of Science, Office of Basic Energy Sciences, under Contract No. W-31-109-ENG-38.

F. List of publications that came out of the subcontracted work

1. T. Buonassisi, A.A. Istratov, M. Heuer, M.A. Marcus, R.Jonczyk, J.Isenberg, B. Lai, Z. Cai, S.Heald, W. Warta, R. Schindler, and E. R. Weber, "Synchrotron-based investigations of the nature and impact of iron contamination in multicrystalline silicon solar cell materials", J.Appl.Phys., accepted for publication.
2. T. Buonassisi, M.A. Marcus, A.A. Istratov, M. Heuer, T. F. Ciszek, B. Lai, Z. Cai, and E.R. Weber, "Analysis of copper-rich precipitates in silicon: chemical state, gettering, and impact on multicrystalline silicon solar cell material", J.Appl.Phys., accepted for publication.
3. O.F.Vyvenko, T.Buonassisi, A.A.Istratov, and E.R.Weber, "X-ray beam induced current/microprobe x-ray fluorescence: synchrotron radiation based x-ray microprobe techniques for analysis of the recombination activity and chemical nature of metal impurities in silicon", J.Phys: Condens. Matter **16**, S141 (2004).
4. A.A.Istratov, T.Buonassisi, R.J.McDonald, A.R.Smith, R.Schindler, J.A.Rand, J.Kalejs, and E.R.Weber, "Metal content of multicrystalline solar cells and its impact on minority carrier diffusion length", J. Appl.Phys. **94**, 6552 (2003).
5. T.Buonassisi, O.F.Vyvenko, A.A.Istratov, E.R.Weber, G.Hahn, D.Sontag, J.P.Rakotoniaina, O.Breitenstein, J.Isenberg, and R.Schindler, "Observation of transition metals at shunt locations in multicrystalline silicon solar cells", J. Appl. Phys. **95**, 1556 (2004).
6. T. Buonassisi, M. Heuer, O.F. Vyvenko, A.A. Istratov, E.R. Weber, Z.Cai, B.Lai, T. Ciszek, and R.Schindler, "Applications of synchrotron radiation x-ray techniques on the analysis of the behavior of transition metals in solar cells and single crystalline silicon with extended defects", Physica B **340-342**, 1137 (2003).
7. O.F.Vyvenko, T.Buonassisi, A.A.Istratov, E.R.Weber, M.Kittler, and W.Seifert, "Application of synchrotron radiation based X-ray microprobe techniques for the analysis of recombination activity of metals precipitated at Si/SiGe misfit dislocations", Journal of Physics: Condensed Matter **14**, 13079 (2002).
8. A.A.Istratov, T.Buonassisi, and E.R.Weber, "The impact of chemical state and thermal stability of metal precipitates on gettering efficiency in silicon", in: proceedings of the 4th international symposium on advanced science and technology of silicon materials (Nov. 22-26, 2004, Kona, Hawaii, USA), p. 473 (published by The Japan Society for the Promotion of Science).
9. T.Buonassisi, A.A.Istratov, and E.R.Weber, "The impact of metal impurity clusters on solar cell performance in multicrystalline silicon", proceedings of the Solar Energy Technologies Program Review Meeting (Denver, CO, October 25-28, 2003).
10. A.A.Istratov, T.Buonassisi, R.J.McDonald, A.R.Smith, R.Schindler, J.Rand, J.P.Kalejs, and E.R.Weber, "Metal content of multicrystalline silicon for solar cells and its impact on minority carrier diffusion length", Solid State Phenomena **95-96**, 175 (2004).
11. T.Buonassisi, O.F.Vyvenko, A.A.Istratov, E.R.Weber, and R.Schindler, "Application of X-ray synchrotron techniques to the characterization of the chemical nature and recombination activity of lifetime limiting defects in solar cells", in "Defects and Impurity Engineered Semiconductors and Devices III", Edited by S. Ashok, J. Chevallier, N.M. Johnson, B.L. Sopori, and H. Okushi, MRS Symp. Proc., Vol. 719, p. 179 (2002).

12. A.A.Istratov, T.Buonassisi, M.A.Marcus, T.F.Ciszek, and E.R.Weber, "Dependence of precipitation behavior of Cu and Ni in CZ and multicrystalline silicon on cooling conditions", in: "14th workshop on Crystalline Silicon Solar Cells & Modules: Materials and Processes", Editor: B.L.Sopori, NREL, Golden, CO, 2004, p.165.
13. T.Buonassisi, A.A.Istratov, T.F.Ciszek, D.W.Cunningham, A.Gabor, R.Jonczyk, R.Schindler, A.Upadhyaya. B.Lai, Z.Cai, M.A.Marcus, and E.R.Weber, "Differences and similarities between metal clusters in mc-Si materials from different manufacturers", in: "14th workshop on Crystalline Silicon Solar Cells & Modules: Materials and Processes", Editor: B.L.Sopori, NREL, Golden, CO, 2004, p.226.
14. T.Buonassisi, A.A.Istratov, M.A.Marcus, and E.R.Weber , "Aluminum gettering and dissolution of Cu_3Si precipitates in silicon", in: "14th workshop on Crystalline Silicon Solar Cells & Modules: Materials and Processes", Editor: B.L.Sopori, NREL, Golden, CO, 2004, pp.222.
15. T.Buonassisi, M.A.Marcus, A.A.Istratov, M.Heuer, T.F.Ciszek, B.Lai, Z.Cai, and E.R.Weber, "Distribution and chemical state of Cu-rich clusters in silicon", in: "14th workshop on Crystalline Silicon Solar Cells & Modules: Materials and Processes", Editor: B.L.Sopori, NREL, Golden, CO, 2004, p. 161.
16. A.A.Istratov, T.Buonassisi, W.Huber, and E.R.Weber, "Evidence for segregation of iron at grain boundaries in polycrystalline and multicrystalline silicon", in: "14th workshop on Crystalline Silicon Solar Cells & Modules: Materials and Processes", Editor: B.L.Sopori, NREL, Golden, CO, 2004, p. 230.
17. T.Buonassisi, A.A.Istratov, and E.R.Weber, "Transition metals in multicrystalline solar cells: understanding the nature, origins, and impacts of metal contamination in mc-Si and minimizing its impact on solar cell performance", in: "14th workshop on Crystalline Silicon Solar Cells & Modules: Materials and Processes", Editor: B.L.Sopori, NREL, Golden, CO, 2004, p. 17.
18. T.Buonassisi, M.Heuer, A.A.Istratov, M.A.Marcus, R.Jonczyk, B.Lai, Z.Cai, J.Isenberg, W.Warta, R.Schindler, and E.R.Weber, "Impact of iron contamination in multicrystalline silicon solar cells: origins, chemical states, and device impacts", to be published in the proceedings of the 19th photovoltaic solar energy conference (Paris, France, June 2004)
19. T.Buonassisi, M.Heuer, A.A.Istratov, E.R.Weber, Z.Cai, B.Lai, M.Marcus, J.Lu, G.Rozgonyi, R.Schindler, R.Jonczyk, and J.Rand, "Statistically meaningful data on the chemical state of iron precipitates in processed multicrystalline silicon using synchrotron-based x-ray absorption spectroscopy", in: "13th workshop on crystalline silicon solar cell materials and processes", editor: B.L.Sopori, NREL, Golden, CO, 2003, p. 96.
20. O.F.Vyvenko, T.Buonassisi, A.A.Istratov, and E.R.Weber, "Experimental procedure for determination of the depth of metal clusters in XBIC/μ-XRF mapping of metal clusters in silicon solar cells", in: "13th workshop on crystalline silicon solar cell materials and processes", editor: B.L.Sopori, NREL, Golden, CO, 2003, p.102.
21. A.A.Istratov, T.Buonassisi, R.J.McDonald, A.R.Smith, R.Schindler, J.A.Rand, J.Kalejs, and E.R.Weber, "Neutron activation analysis study of metal content of multicrystalline slicon for cost-efficient solar cells", in: "13th workshop on crystalline silicon solar cell materials and processes", editor: B.L.Sopori, NREL, Golden, CO, 2003, p. 158.
22. T.Buonassisi, O.F.Vyvenko, A.A.Istratov, E.R.Weber, G.Hahn, D.Sontag, J.P.Rakotoniaina, O.Breitenstein, J.Isenberg, and R.Schindler, "Assessing the role of transition metals in shunting mechanisms using synchrotron-based techniques", 3rd World Photovoltaic Specialists Conference (WCPEC-3), Osaka, Japan (2003).

23. A.A.Istratov, T.Buonassisi, E.R.Weber, R.J.McDonald, A.R.Smith, R.Schindler, J.Isenberg, J.Kalejs, J.Rand, P.Geiger, G.Hahn, J.P.Rakotoniaina, and O.Breitenstein, "Impact of metal impurities on solar cell performance", proceedings of the NCPV and Solar Program Review Meeting (March 24-26, 2003), pp. 228-230, published by NREL, Golden, Colorado, 2003. Available in electronic form, NREL/CD-520-33586.
24. O.F.Vyvenko, T.Buonassisi, A.A.Istratov, and E.R.Weber, "Application of synchrotron radiation based X-ray microprobe technique for the analysis of recombination activity of metals precipitated at Si/SiGe misfit dislocations", in "12th workshop on crystalline silicon solar cell materials and processes", editor: B.L.Sopori, NREL, Golden, CO, 2002, p. 111.
25. T.Buonassisi, O.F.Vyvenko, A.A.Istratov, E.R.Weber, R.Schindler, and G.Hahn, "Analysis of shunts in multicrystalline silicon solar cells using microprobe X-ray fluorescence technique", in "12th workshop on crystalline silicon solar cell materials and processes", editor: B.L.Sopori, NREL, Golden, CO, 2002, p. 266.
26. O.F.Vyvenko, T.Buonassisi, A.A.Istratov, and E.R.Weber, "Application of X-ray fluorescence technique to studies of aluminum gettering in silicon", in "12th workshop on crystalline silicon solar cell materials and processes", editor: B.L.Sopori, NREL, Golden, CO, 2002, p. 271.

REPORT DOCUMENTATION PAGE

Form Approved
OMB No. 0704-0188

PLEASE DO NOT RETURN YOUR FORM TO THE ABOVE ORGANIZATION.

1. REPORT DATE *(DD-MM-YYYY)*	2. REPORT TYPE	3. DATES COVERED *(From - To)*
February 2005	Final Subcontract Report	October 2001–December 2004

4. TITLE AND SUBTITLE
Efficiency Improvement of Crystalline Solar Cells:
Final Subcontract Report, October 2001–December 2004

5a. CONTRACT NUMBER
DE-AC36-99-GO10337

5b. GRANT NUMBER

5c. PROGRAM ELEMENT NUMBER

6. AUTHOR(S)
E.R. Weber

5d. PROJECT NUMBER
NREL/SR-520-37578

5e. TASK NUMBER
PVA52201

5f. WORK UNIT NUMBER

7. PERFORMING ORGANIZATION NAME(S) AND ADDRESS(ES)
University of California, Berkeley
Berkeley, California

8. PERFORMING ORGANIZATION REPORT NUMBER
AAT-2-31605-03

9. SPONSORING/MONITORING AGENCY NAME(S) AND ADDRESS(ES)
National Renewable Energy Laboratory
1617 Cole Blvd.
Golden, CO 80401-3393

10. SPONSOR/MONITOR'S ACRONYM(S)
NREL

11. SPONSORING/MONITORING AGENCY REPORT NUMBER
NREL/SR-520-37578

12. DISTRIBUTION AVAILABILITY STATEMENT
National Technical Information Service
U.S. Department of Commerce
5285 Port Royal Road
Springfield, VA 22161

13. SUPPLEMENTARY NOTES
NREL Technical Monitor: R. Matson

14. ABSTRACT *(Maximum 200 Words)*

The approach in this subcontract was to use unique analytical tools available at Berkeley to perform systematic fundamental physical studies of the distribution and chemical state of metal clusters in a variety of multicrystalline silicon materials. Two analytical techniques were essential for the success of this project. The total metal concentration in the areas of multicrystalline silicon with high and low lifetime was determined by neutron activation analysis, a technique that involves irradiation of a sample with neutrons in a nuclear reactor and analysis of its residual radioactivity. The distribution and chemical state of metal clusters was characterized by synchrotron radiation-based X-ray microscopes available at the Advanced Light Source (Beamlines 10.3.1 and 10.3.2) at Lawrence Berkeley National Laboratory and Advanced Photon Source (Beamlines 2-ID-D and 20-ID-B) at Argonne National Laboratory.

15. SUBJECT TERMS
PV; module; solar cells; manufacturer; metal clusters; multicrystalline silicon; synchrotron radiation; X-ray absorption microspectroscopy (μ-XAS); microprobe X-ray fluorescence (μ-XRF); in-situ; X-ray-beam-induced current measurements (XBIC); float zone;

16. SECURITY CLASSIFICATION OF:			17. LIMITATION OF ABSTRACT	18. NUMBER OF PAGES	19a. NAME OF RESPONSIBLE PERSON
a. REPORT	b. ABSTRACT	c. THIS PAGE			19b. TELEPONE NUMBER (*Include area code)*
Unclassified	Unclassified	Unclassified	UL		

Standard Form 298 (Rev. 8/98)
Prescribed by ANSI Std. Z39.18